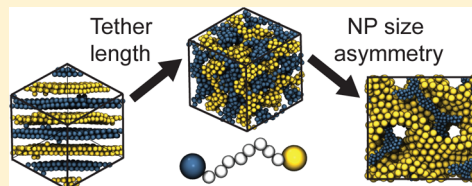


Phase Behavior and Complex Crystal Structures of Self-Assembled Tethered Nanoparticle Telechelics

Ryan L. Marson,[†] Carolyn L. Phillips,[‡] Joshua A. Anderson,[§] and Sharon C. Glotzer*,^{*,†,‡,§}

[†]Materials Science and Engineering, [‡]Department of Applied Physics, and [§]Chemical Engineering, University of Michigan, Ann Arbor, Michigan 48109, United States

ABSTRACT: Motivated by growing interest in the self-assembly of nanoparticles for applications such as photonics, organic photovoltaics, and DNA-assisted designer crystals, we explore the phase behavior of tethered spherical nanoparticles. Here, a polymer tether is used to geometrically constrain a pair of nanoparticles creating a tethered nanoparticle “telechelic”. Using simulation, we examine how varying architectural features, such as the size ratio of the two end-group nanospheres and the length of the flexible tether, affects the self-assembled morphologies. We demonstrate not only that this hybrid building block maintains the same phase diversity as linear triblock copolymers, allowing for a variety of nanoparticle materials to replace polymer blocks, but also that new structures not previously reported are accessible. Our findings imply a robust underlying ordering mechanism is common among these systems, thus allowing flexibility in synthesis approaches to achieve a target morphology.



KEYWORDS: *Tethered nanoparticles, self-assembly, DNA nanotechnology, block copolymer, gyroid*

Materials with features engineered at the micrometer to nanometer scale are in high demand. Photonic and meta-materials require structures with finely tuned band gaps.^{1–3} Computer chip manufacturers need materials with sharply defined interfaces at the sub-20 nm scale to increase transistor counts and reduce power density.⁴ Photovoltaic devices need precisely structured materials with maximal interfacial area to facilitate electron–hole pair disassociation in the active layer.⁵ Complex crystal structures, such as the gyroid, are candidates for nanoscale chiral beam splitters⁶ and efficient electrochromic devices.⁷ “Bottom-up” design techniques, such as self-assembly (SA), provide a promising method⁸ for synthesizing precisely engineered materials by leveraging advances in nanoparticle fabrication by varying size, shape, functionality, and interaction mechanisms.^{9,10}

Tethered nanoparticles (TNPs) have been introduced conceptually as a new class of nanoparticle building block, capable of self-assembling materials with finely controlled complex structure.¹¹ TNPs are a class of building block analogous to block copolymers (BCP) and surfactants; they can be thought of either as a short BCP with one or more block segment(s) replaced by a NP, or a surfactant with a NP headgroup. As shape amphiphiles, TNPs can have the same topological diversity as BCPs (linear, star, ring, branched, comb, and so forth), while adding the capacity to engineer the structure and chemical functionality of the NP. In this way, TNPs provide additional versatility due to the huge variety of experimentally feasible candidate nanoparticles and the relative ease with which nanoparticle features can be controlled at the 2–100 nm length scale. Most importantly, TNPs can be controlled with interaction mechanisms beyond the immiscibility characteristic of amphiphiles. Experimental realizations of TNPs include DNA-tethered nanoparticles^{12–23} and giant surfactants.^{24–28} Moreover, it has recently become possible to

synthesize gram quantities of giant surfactant TNPs through advances in synthetic “click” chemistry,²⁹ enabling modular design of building block architectures.²⁷

Computer simulations predict that TNP systems form a variety of ordered phases.^{11,30–44} These phases include structures similar to those found in di- and triblock copolymers such as lamellar sheets, hexagonally packed cylinders, and network phases (gyroids and diamond phases); additionally, morphologies not previously observed in polymer systems have been reported, such as zincblende or simple cubic arrangement micelles within continuous NP networks.^{39,40} Combining the flexibility of design and material choice of TNPs with the phase diversity possible in star polymers^{45–48} offers further avenues to engineer materials with complex mesostructured morphologies.^{49,50}

To date, these simulations have been restricted to TNPs comprised of a single nanoparticle bonded to one,^{30,32–35,38,41,42} two,^{39,40} or several flexible polymer chains.^{11,31} In this paper, we examine a system of tethered nanoparticle telechelics (TNPTs). We define a TNPT as a hybrid building block composed of two nanoparticles whose shapes and sizes can be selected independently and are linked by a short, flexible polymer chain. With the enormous diversity of NP shape now possible⁹ and the complex motifs possible for these shapes,⁵¹ the design space of TNPTs is practically infinite. The simplest realization of this building block is composed of two spherical NPs connected by a single tether. We examine how the relative size ratios of a spherical headgroup and the length of their joining tether determine the self-assembled structure.

Published: March 18, 2014



Model. We utilize a minimal coarse-grained model used in previous works to study the phase behavior of the TNPT.^{32,39,40,42} NPs are modeled as beads of diameter 1.0σ , 2.0σ , 3.0σ , or 4.0σ ; tethers are modeled as chains of beads of diameter 1.0σ , which is the persistence length of a polymer segment. We consider NPs of a single TNPT to be generally two different particle types, as shown in Figure 1a. To mimic

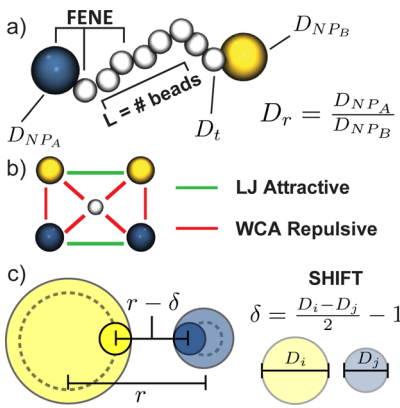


Figure 1. The TNPT model. (a) Four different tether lengths are explored: $L = 2, 4, 6$, and 8 beads. For each choice of L , three different diameter ratios are used: $D_r = D_{NP_A}/D_{NP_B} = 1.0, 0.6$, and 0.5 . (b) NPs interact with like species via an SLJ potential. A shifted WCA models a repulsion between unlike species. The nanoparticle is bonded to a tether bead by a FENE spring; additionally, tether beads are also connected by FENE springs. (c) Description of the shifted LJ and WCA potentials. The potential is shifted by δ and evaluated at a distance $r - \delta$.

immiscibility between NPs, those of the same type have an attractive interaction, while all other interactions are volume excluding. To model interactions we use a radially shifted Lennard-Jones (SLJ) potential, which shifts the potential to the surface of the particle. Figure 1b illustrates the interactions between particle types.

The radially shifted Lennard-Jones pair potential is

$$V_{ij}^{\text{SLJ}}(r) = 4\epsilon_{ij} \left[\left(\frac{\sigma_{ij}}{(r - \delta)} \right)^{12} - \left(\frac{\sigma_{ij}}{(r - \delta)} \right)^6 \right] \quad (1)$$

The attractive interaction potential, which is applied between nanoparticle pairs of the same type (NP_A-NP_A , NP_B-NP_B), is

$$U_{ij}^{\text{attractive}}(r) = \begin{cases} V_{ij}^{\text{SLJ}}(r) - V_{ij}^{\text{SLJ}}(r_{\text{cut}}^{\text{SLJ}}) & r < r_{\text{cut}}^{\text{SLJ}} + \delta \\ 0 & r \geq r_{\text{cut}}^{\text{SLJ}} + \delta \end{cases} \quad (2)$$

The units of interaction strength ϵ_{ij} are $\epsilon_{ij} = 1.0\epsilon$ between all particle pairs, the units of diameter for all beads in the system are $\sigma_{ij} = 1.0\sigma$, $\delta = [(D_i - D_j)/2] - 1$ is the magnitude of the shift (where D_i and D_j are the diameters of beads i and j , respectively), and $r_{\text{cut}}^{\text{SLJ}} = 2.5\sigma$. This form of the potential assures that there is no softening of the potential when accommodating systems of NPs with different diameters.

For unlike pairs (NP_A-NP_B , NP_A-t , NP_B-t , $t-t$) we use a shifted Weeks-Chandler-Anderson (SWCA) potential.⁵² SWCA is the LJ potential shifted by ϵ and with $r_{\text{cut}}^{\text{WCA}} = 2^{1/6}\sigma$

$$U_{ij}^{\text{repulsive}}(r) = \begin{cases} V_{ij}^{\text{SLJ}}(r) - V_{ij}^{\text{SLJ}}(r_{\text{cut}}^{\text{WCA}}) & r < r_{\text{cut}}^{\text{WCA}} + \delta \\ 0 & r \geq r_{\text{cut}}^{\text{WCA}} + \delta \end{cases} \quad (3)$$

Nanoparticles are bonded to end tether beads with finitely extensible nonlinear elastic (FENE) springs

$$U_{ij}^{\text{FENE}}(r) = -\frac{1}{2}kR_0^2 \ln \left[1 - \left(\frac{r - \delta}{R_0} \right)^2 \right] \quad (4)$$

with $k = 30(\epsilon/\sigma^2)$ as the spring constant and $R_0 = 1.5\sigma$ equal to the maximum allowed separation between the two particles, which avoids artificial tether crossing. Additionally, FENE springs are used to bond individual beads of the tether.

For the TNTP, σ is the individual bead diameter, m is the bead mass, and ϵ is the LJ interaction strength, making the dimensionless time of the system $t = (m\sigma^2/\epsilon)^{1/2}$. Temperature is given by $T^* = k_b T/\epsilon$ and controls the degree of immiscibility of individual particles. The volume fraction, ϕ , of the system is determined by dividing the total excluded volume of all beads by the total volume of the box.

Systems are simulated in an implicit solvent within the NVT ensemble, using Brownian Dynamics⁵³ (BD), which obviates the need for explicit solvent (and thus reduces the computational workload). Particle trajectories are governed by the Langevin equation, given by

$$m_i \ddot{r}_i(t) = \mathbf{F}_i^C(\mathbf{r}_i(t)) + \mathbf{F}_i^R(t) - \gamma_i \mathbf{v}_i(t) \quad (5)$$

where m_i is the particle's mass, r_i is the position, F_i^C is the conservative force on the particle, F_i^R is a random force, v_i is the particle velocity, and γ_i is the particle's friction coefficient. The friction coefficient is $\gamma_i = -6\pi\eta a$, where η is the solvent viscosity and a is the particle diameter. F_i^C is the conservative force established by the SLJ and FENE potential fields. The F_i^R satisfies the fluctuation-dissipation theorem. The combined effect of the γ_i and the F_i^R is to couple particles to a nonmomentum-conserving heat bath.

Simulations are initialized with $N = 1000$ TNPTs randomly placed in a periodic, cubic box. The system is randomized by raising the temperature well above the order-disorder transition temperature, $T^* \gg T_{\text{ODT}}^*$ for 10 million time steps. All simulations begin dilute and are compressed to the desired volume fraction over 10^4 time steps by uniformly scaling the box dimensions. The system temperature is lowered by $\delta T^* = 0.05$ and run for 20 million time steps at each increment to a final temperature of $T^* = 0.25$. All simulations use a time step $\Delta t = 0.005(m\sigma^2/\epsilon)^{1/2}$. Each simulation is repeated 10 times with different random initial conditions. Simulations are performed using the Highly Optimized Object-Oriented Molecular Dynamics (HOOMD)-Blue software package,⁵⁴⁻⁵⁶ a GPU-based MD code. In total, the study contains over 480 individual simulations, encompassing over 10^4 hours of GPU time.

All phases are identified through a combination of visual inspection, diffraction pattern, radial distribution function (RDF), and bond order diagram (BOD) analysis. To obtain unit cells, micelle and network node locations are determined by using Gaussian blurring and thresholding on particle positions. Blurred particle positions are averaged over at least 100 frames, which are dumped every $1000\Delta t$. Micelle and network node locations are then determined by constructing a

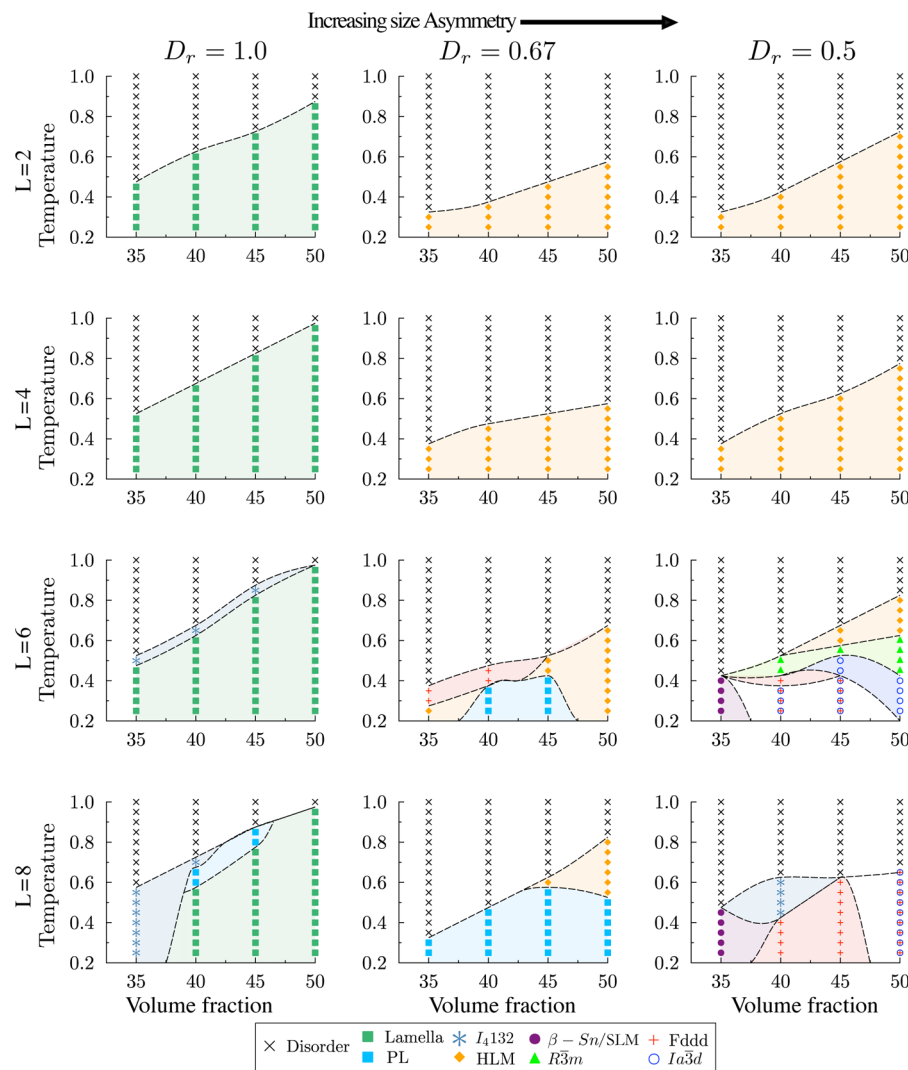


Figure 2. Phase diagram. At top, each of the three diameter ratios (D_r) are listed from most to least size-symmetric; tether length (L) increases from top to bottom. Each diagram contains a listing of phases found between 35 and 50% volume fraction (ϕ) over a wide temperature range. Regions are shaded and separated with dotted lines to guide the reader. Overlapping symbols indicate multiple stable phases in a region.

cluster centroid from the blurred and averaged density grid. Unit cells are then compared to perfect crystal structures (obtained, for example, from the Naval Crystal Database⁵⁷) for final structure determination. Where possible, system snapshots are rendered with individual nanoparticle beads. In some cases, however, the larger nanoparticle species is rendered as a transparent isosurface, so that ordering in the smaller species is not obscured.

The simulated nanoparticles (NP) are assigned a diameter $D_{NP} = 1\sigma, 2\sigma, 3\sigma$, or 4σ . In all figures, the smaller nanosphere is labeled nanoparticle A (NP_A) and colored blue; the larger is labeled nanoparticle B (NP_B) and colored yellow. We simulate three nanoparticle diameter ratios, $D_r = D_{NP_A}/D_{NP_B} = 1.0, 0.67$, and 0.5, and four tether lengths, $L = 2, 4, 6$, and 8 beads of diameter 1σ . Every system was simulated at volume fractions $\phi = 35, 40, 45$, and 50%; additionally, where noted, some cases were investigated at lower volume fractions. Each temperature schedule represents at least ten separate simulations. All phases reported occurred in three or more of the ten independent simulations. Each phase contains at least two unit cells per box direction (8 total unit cells), aside from the $Ia\bar{3}d$ and $Fdd\bar{d}$ networks, which contain one unit cell.

During a simulation run, structures can rearrange within the box to accommodate their geometry. However as the complexity of the structure increases, this requires a larger fluctuation of the system. For structures with a single lattice parameter, such as lamellae, the structure can reorient along an axis of the box that satisfies its lattice parameter. Structures with two lattice parameters (e.g., hexagonal and tetragonal tubes) can also reorient to satisfy both lattice parameters. For structures periodic in all three dimensions, all three lattice parameters must be close to correct to accommodate an integer number of unit cells (such structures typically withstand a small amount of compression/stretching). When the simulated structure has unequal lattice parameters, it must be able to orient within the box so as to satisfy those parameters. In all of the simulations we report here, this is indeed the case.

In some parts of the phase diagram, multiple phases were observed. In the thermodynamic limit, we expect only a single phase to be present. Distinguishing which phase represents the global free energy minimum, however, is beyond the scope of the present study. We make note of these competing structures in the Results and examine reasons for their competing stability in the Discussion.

Results. We report several phases that are new to the TNP design-space and identify new analogs to several structures that have been previously reported in TNP simulations where the building blocks are comprised of a single NP and one or two tethers.^{32,36,37,39,40,42} Figure 2 shows a phase diagram of the observed structures. Two phases, body-centered cubic (bcc) spherical micelles and tetragonal long micelles, were found for parameters that fell outside the parameter range of Figure 2.

Micelle in Network Phases. β -Sn Micelles in Network. For tether lengths of $L = 6$ and $L = 8$ at $\phi = 35\%$ and $D_r = 0.5$, the TNPT assembles a β -Sn (with an elongated *c*-axis) phase, as shown in Figure 3a. Figure 3b shows the particle centroids

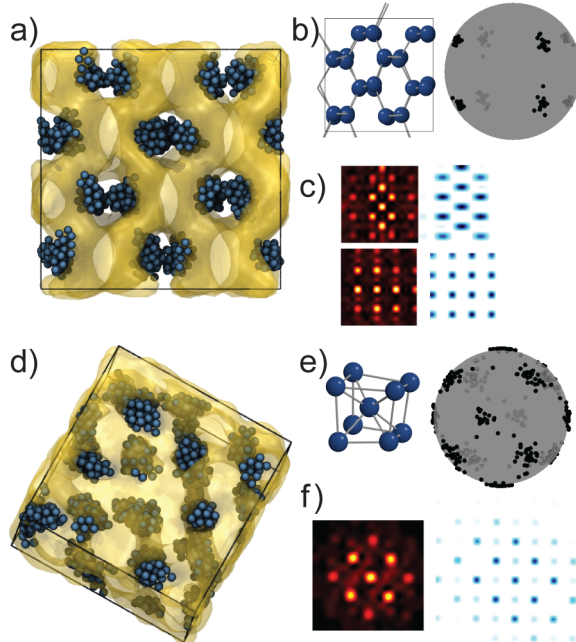


Figure 3. Micelle phases. (a) β -Sn micelles. (b) (left) The micelle centroids and (right) a BOD for the nearest neighbor centroids. (c) The diffraction pattern of the centroids (left) and an ideal β -Sn crystal. (d) bcc micelles. (e) A unit cell constructed from the micelle centroids and a BOD for the nearest neighbor centroids. (f) The diffraction pattern of the centroids (left) and an ideal bcc crystal.

extracted by Gaussian filtering and the BOD of the nearest neighbor centroids. The centroid diffraction pattern is shown from two different symmetry axes, Figure 3c (left), and compared to the diffraction pattern of an ideal β -Sn crystal structure, Figure 3c (right).

In this phase, NP_A form spherical micelles that decorate a β -Sn lattice, while NP_B form a continuous β -Sn network. As is characteristic of the β -Sn crystal structure, the micelles are offset (do not lie on the same line) and alternate through the crystal structure from two symmetry axes. Because this β -Sn phase has an elongated *c*-axis the BOD does not indicate neighbors at the north and south “poles”, as would be found for the BOD of an ideal β -Sn crystal structure. NP_B forms a continuous network phase that surrounds the micelles. This phase is the tetragonal analog to the diamond crystal, compressed in the “*c*” direction; the ideal β -Sn crystal structure is further compressed in the “*c*” direction. The network phase is shown as a yellow transparent isosurface in Figure 3a.

bcc Micelles in Network. For tether lengths of $L = 2$ at $\phi = 30, 35$, and 45% , and $L = 4$ at $\phi = 45\%$, with $D_r = 0.5$, the TNPT assembles a bcc micelle phase, shown in Figure 3d. This data is not shown in Figure 2, as this phase was found in a small set of simulations where, despite the same ratio of 1/2, the absolute sphere sizes are twice as big ($D_r = (2\sigma/4\sigma)$, instead of $(1\sigma/2\sigma)$).

In the bcc phase, NP_A beads form micelles, which decorate a bcc lattice. Figure 3e shows a bcc unit cell extracted from the simulation data and the BOD of the micelle centroids. The diffraction pattern of the 4-fold axis of the centroid is shown in Figure 3f (left), along with the diffraction pattern of a perfect bcc crystal structure. NP_B form a network that surrounds the lattice. The network phase is shown as a yellow transparent isosurface in Figure 3d.

Network Phases. Gyroid Networks. The TNPT assembles two types of gyroid structures, the alternating gyroid (AG) and the double gyroid (DG).

The AG forms at tether lengths of $L = 6$ for $\phi = 35, 40$, and 45% as well as at $L = 8$ for $\phi = 35$ and 40% for $D_r = 1.0$. The AG is also found for $\phi = 40\%$ at $L = 8$ and $D_r = 0.5$. The AG has symmetry $I4_132$ (No. 217) and is composed of two interpenetrating gyroid networks of opposite chirality composed of NP_A and NP_B respectively, as shown in Figure 4b. The polymer tether fills the dividing space between the two networks. The NP_A and NP_B domains are shown on the top and bottom right of Figure 4d, respectively. Within a single gyroid network, three edges of the network connect at a node. Nodes connected by an edge are rotated 70.5 degrees relative to each other.⁵⁸ The nodes formed in both the NP_A and NP_B gyroid can be seen on the right of Figure 4b.

The DG forms for tether lengths of $L = 6$ at $\phi = 40\%, 45\%, 50\%$ and for $L = 8$ at $\phi = 50\%$ at $D_r = 0.5$; it is shown in Figure 4a. In contrast to the AG, in the DG both halves of the interpenetrating gyroid network are composed of NP_A (Figure 4a, top right) and are surrounded by the tether. Thus, the DG of symmetry $Ia\bar{3}d$ (No. 230) has an inversion symmetry that the AG does not. The NP_B (Figure 4a, bottom right) forms the minimal surface that divides the two gyroid networks.

Per Figure 2, at $L = 6$ there is an order-order phase transition between the DG and either the hexagonally long micelle (HLM) or $R\bar{3}m$ network phase, but at $L = 8$ the DG forms spontaneously from a disordered system. In all regions except for $L = 6$ at $\phi = 50\%$, the DG competes for stability with the $Fddd$ network.

***Fddd* Network.** An *Fddd* network phase (space group No.70) forms at tether length $L = 6$, $\phi = 35$ and 40% for $D_r = 0.67$, and at $\phi = 40\%$ for $D_r = 0.5$. At a tether length of $L = 8$, the *Fddd* network forms at $\phi = 40, 45$, and 50% for $D_r = 0.5$.

As shown in Figure 4e, NP_A form a continuous network where three edges meet at each node; each node and edge group lie in the same plane. Two of the edges connect to a node with edges in the same plane, while the third edge connects to a node rotated into a new plane. This pattern of node connections combines the patterns of the perforated lamellae (PL) (same plane) and DG/AG (different plane) network structures.⁵⁸ NP_B forms a surface that surrounds the network. The NP_A and NP_B domains are shown on the right of Figure 4e.

The *Fddd* network is a highly anisotropic, orthorhombic structure with three different lattice parameters.⁵⁹ As can be seen in Figure 4c, to satisfy these anisotropic lattice parameters

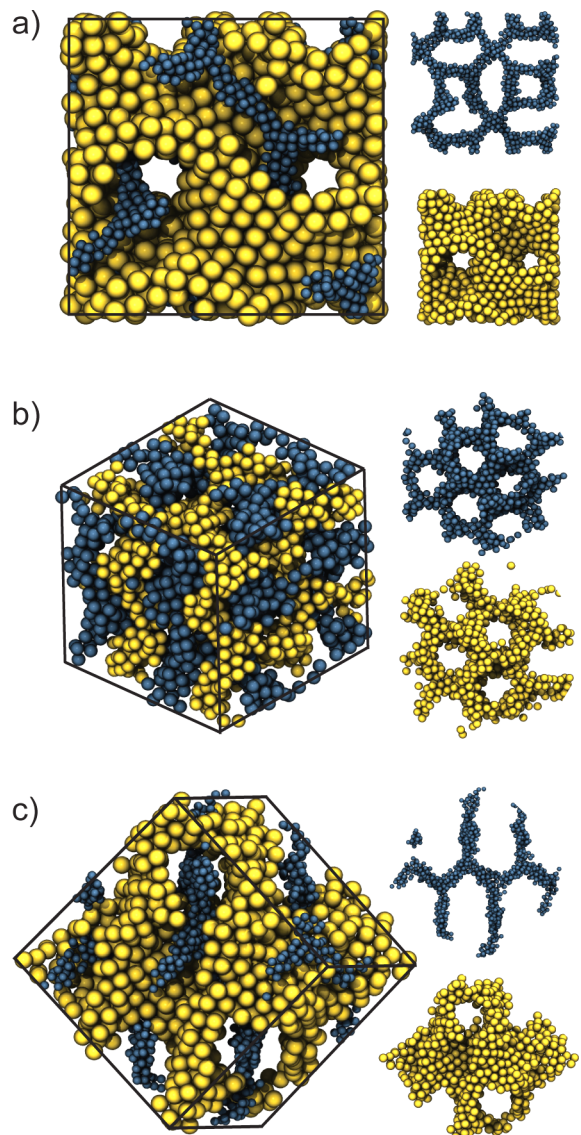


Figure 4. Network phases. Three network structures. (a) $Ia\bar{3}d$ (space group No. 230) double gyroid. (b) $I4_132$ (space group No. 214) alternating gyroid. (c) $Fddd$ (space group No. 70) $Fddd$ network.

the phase must both choose a noncubic tiling and orient along a longer axis of the cubic simulation box.

Per Figure 2, at $D_r = 0.67$ there is an order–order phase transition between the $Fddd$ phase and PL or HLM. At $D_r = 0.5$, there is an order–order phase transition between the $Fddd$ phase and $R\bar{3}m$. In several regions, the $Fddd$ network competes for stability with the DG.

Long Micelle Phases. Tetragonally Arranged, Alternating Long Micelles. For a tether length of $L = 8$ at $\phi = 25\%$, $D_r = 1.0$, the TNPT system forms a tetragonal packing of long cylindrical micelles (TLM). This phase was found in a small set of simulations outside the range shown in Figure 2. This was the only ordered phase observed for $\phi < 35\%$.

In this phase, both NP_A and NP_B form long micelles, as seen in Figure 5f. The LM arrange tetragonally, rather than hexagonally, and alternate NP_A and NP_B. The polymer tether fills the space between the LM.

Hexagonally Arranged, Long Micelles. For a tether length of $L = 2$ and 4, $\phi = 35\text{--}50\%$, $D_r = 0.67$ and 0.5, the TNPT

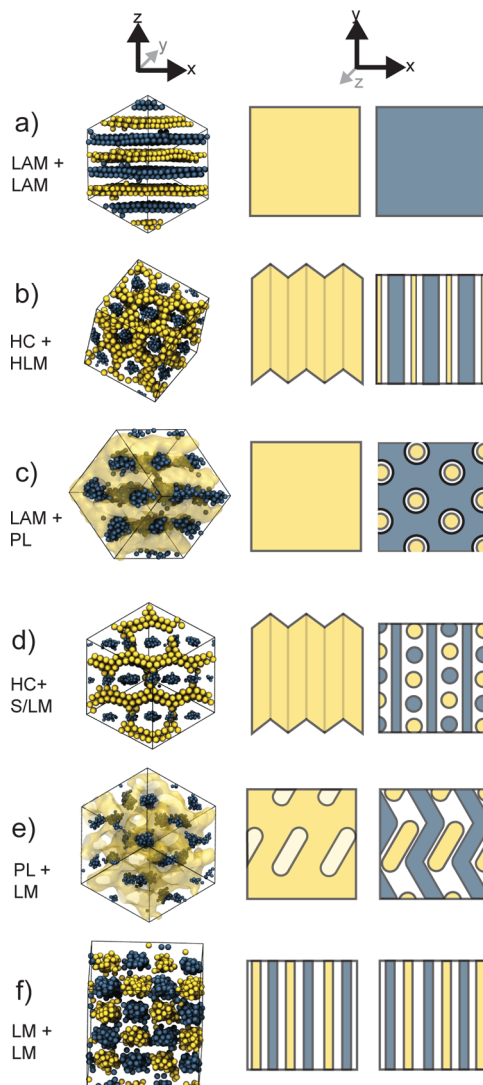


Figure 5. LAM, PL, and LM phases. The left column shows simulations results for the following phases: (a) lamellar phase, (b) honeycomb plus long micelle phase, (c) lamellar plus perforated lamellar phase, (d) lamellar plus short/long micelle phase, (e) ($R\bar{3}m$) perforated lamellar plus long micelle phase, and (f) tetragonally arranged long micelle phase. The middle and right column illustrate neighboring cross sections of the phase.

system forms hexagonally arranged long micelles (HLM). The phase also forms for a tether length of $L = 6$, $\phi = 35, 45, 50\%$ and $L = 8$, $\phi = 45$ and 50%, for $D_r = 0.67$, and $L = 6$, $\phi = 45$ and 50%, for $D_r = 0.5$.

In the HLM phase, NP_A form LMs that are hexagonally arranged, as shown in Figure 5b. The tethers form a shell around the LMs. NP_B forms a honeycomb (HC) shaped bilayer around the LM. As the tether increases in length, the shell formed around the LM becomes thicker.

As seen in Figure 2, for $L = 2$ and $L = 4$, $D_r = 0.67$ and 0.5, HLM was the only stable phase found. At $L = 6$ and 8, there is an order–order phase transition between HLM and PL phases, the $Fddd$ network, and $R\bar{3}m$.

$R\bar{3}m$ Micelles. A network phase of space group $R\bar{3}m$ (space group No. 166) forms at a tether length $L = 6$ at $\phi = 40, 45, 50\%$, $D_r = 0.5$.

Within this phase, NP_A forms a weaving long micelle type structure. These structures have nearly straight sections that

weave around the surface formed by NP_B , forming distinct “kinks” followed by persistent straight sections. The effect of these kinks is to create a “square-wave”-like long micelle, as shown in Figure 5e. This structure shares the same space group with hexagonally perforated lamellar structures of type ABC packing (HPL_{ABC}), but is a different structure.⁶⁰

Honeycomb with Spherical and Long Micelles. For tether lengths of $L = 6$ and $L = 8$, at $\phi = 35\%$, and $D_r = 0.5$ the TNPT assembles a honeycomb with spherical and long micelle (HC/SLM) phase, as shown in Figure 5d. This phase forms in the same region of the phase diagram for the same thermodynamic parameters as the β -Sn micelles.

In this phase, NP_B forms a honeycomb-like structure with lateral perforations that are perpendicular to the long axis of the honeycomb. NP_A forms a set of alternating spherical and long micelles; long micelles sit in the center of HC cells, while spherical micelles occupy the lateral perforations. The tether forms a shell around the micelles, filling the space between NP_A and NP_B .

Lamellar Phases. Lamellae. For $D_r = 0.5$ lamellar (LAM) sheets are the most prevalent structure. At tether lengths $L = 2$ and $L = 4$ this is the only ordered phase present at all ϕ . For $L = 6$, the AG forms at intermediate T^* with a LAM configuration stable at low T^* . At the longest tether length, $L = 8$, LAM structures form at intermediate to high T^* , remaining stable throughout the simulation.

The LAM structure is composed of two nanoparticle domains that each form a layer spanning the length of the box. An example of this type of structure is shown as the equilibrated phase in Figure 5a. Nanoparticle domains alternate in chemical specificity. The spacing between layers in the LAM structure is determined by the length of the polymer tether; increasing tether length increases the spacing between layers.

Perforated Lamellae. Perforated lamellae (PL) form for $D_r = 0.67$ at both the $L = 6$ and $L = 8$ tether lengths. In the $L = 6$ tether length case, HPL form at $\phi = 40$ and 45% for low T^* . Increasing the tether length to $L = 8$, we also see a prevalence of PL structures forming at $\phi = 35, 40, 45$, and 50%; here the HPL form at intermediate T^* .

As shown in Figure 5c, NP_A forms a set of lamellar sheets with perforations. NP_B forms a honeycomb-like structure that surrounds the PL. This HC structure contains lateral perforations, which accommodate the PL. This phase is similar to the HLM phase. For NP_A , these connections occur between tubes, laterally, to become PL; for NP_B , layers connect vertically to form a HC-like structure.

Discussion. The TNPT design space contains the same set of structures found in linear triblock copolymer systems. All linear TBCP phases reported as equilibrium or metastable phases in the literature⁵⁸ appear in our phase diagram, including bcc micelles, hexagonal tubes, tetragonal alternating tubes, both AB and ABC stacked perforated lamellar sheets, standard lamellar sheets, the Fddd structure, and both alternating ($I4_132$) and double ($Ia\bar{3}d$) gyroids.^{58,61–65} This is significant in that it predicts that NPs from a variety of materials can take the place of the usual polymer end blocks while maintaining the same phase diversity.

Symmetry (or asymmetry) in the size of the NP end groups usually results in the assembly of microphases that are likewise symmetric (or asymmetric) with respect to the end groups. For $D_r = 1.0$, we find only symmetric phases, that is, phases invariant to exchanging the two end groups. These phases are tetragonally arranged long micelles, the AG, and AB lamellar

sheets. As an example, in the AG each of the two interpenetrating chiral networks of the gyroid is composed of a single nanoparticle species. For $D_r = 0.67$ and $D_r = 0.5$, all phases found are asymmetric with respect to the end groups. Thus, for the DG a single end group now forms both chiral networks of the gyroid; the other, larger, end group forms the minimal surface that divides the space between interpenetrating networks. The single exception is an AG that forms with $D_r = 0.5$ for $L = 8$ at $\phi = 40\%$. In this case, the volume fractions of the two end groups are asymmetric. However, this phase is only present at high T where the effective volume of the smaller nanoparticle domain is larger due to large thermal fluctuations. At low T^* , the system stabilizes an Fddd phase, which is again asymmetric with respect to the end groups.

Increasing the length of the polymer tether provides the TNPT system with the configurational freedom necessary to adopt an increasing number of complex phases. At short tether lengths, we find only a single ordered phase at each diameter ratio—lamellar sheets for $D_r = 1.0$ and hexagonally arranged long micelles in a honeycomb network for $D_r = 0.67$ and $D_r = 0.5$. TNPT with short tethers are effectively floppy dimers and form phases similar to those observed in sets of asymmetric, softened dumbbells.⁶⁶ At longer tether lengths, several micelle and network phases are present. We also observe order-order transitions, suggesting the configurational entropy added by the longer tether is a significant contribution to the free energy. Also, more of the phases seen in triblock copolymer system are observed in this part of the TNTP phase diagram.⁵⁸

The most complex region of the phase diagram occurs where the diameter ratio is the most asymmetric ($D_r = 0.5$) and the tether length is moderately long ($L = 6$). Throughout the assembly process the system must balance constraints imposed by asymmetry in nanoparticle size and configurational freedom provided by the tether. In this region, the system is best able to balance these constraints, driving the assembly of complex structures.

We note that whereas block copolymer gyroid and Fddd network phases are observed at melt densities in polymer systems, here we find these same structures at considerably lower densities, similar to densities of surfactant and lipid-based systems. Thus, the solvent fraction seemingly plays a large role in stabilizing these morphologies, as immiscibility is the mechanism responsible for the phase separation. In lipid or surfactant systems, however, the double gyroid is comprised of two chiral interpenetrating networks of head groups, and a matrix of tail groups.⁶⁷ In contrast, we report a gyroid where the material of each of the two interpenetrating single gyroid networks can be controlled separately.

The β -Sn micelles in network, the R $\bar{3}m$ long micelles, and honeycomb with spherical and long micelles have not been reported in the triblock copolymer literature to our knowledge. In linear triblock copolymers, the only micelle phase reported is bcc.⁵⁸ All three new phases occur at the most asymmetric diameter ratio, $D_r = 1\sigma/2\sigma = 0.5$. We found that maintaining the same diameter ratio but doubling the volume of the end groups produces a bcc micelle in network phase instead. Both the R $\bar{3}m$ and HC/SLM are mixed lamellar-micellar morphologies.

In several cases, we see competition between two phases in regions of the phase diagram. This occurs due to small differences in free energy between related phases. The perforated lamellar phases, for example, have been proposed to be kinetically arrested, metastable precursors to continuous

network phases, for both block copolymer^{68–70} and TNP systems.^{33,36} The *Fddd* and *Ia* $\bar{3}$ *d* gyroid are, similarly, known to be very close in free energy.⁵⁹ Our simulations were run for tens of millions of time steps for each temperature value reported, but this does not guarantee that the system will find the free energy minimizing structure. Moreover, it is possible that even stable structures can fluctuate out of equilibrium at higher temperatures and not fluctuate back over the duration of a simulation. Deciding which structures are the true equilibrium structures, however, is not the goal of the present study. Rather, we aim to qualitatively understand how tethering can be used as a tool for the creation of complex self-assembled structures.⁹ Thus, we report both stable and robust metastable phases, mindful that metastable structures are desirable⁷¹ or can be important precursors in kinetic transitions to more complex structures like the gyroids.^{36,60,72}

Our simulations predict that replacing the polymer blocks of the BCPs with NPs has two significant effects. First, the conformational entropy of the end group is reduced.^{32,39} Second, when the NPs are confined to an end-group domain of a microphase-separated system, the local packing of the NPs induces order. Microphase separation promotes local icosahedral packing for spherical NPs, for example.^{36,73} As a result, TNP systems can have additional ordering not found in polymer microphase separated systems. By varying the geometry of the NPs, it may be possible to realize different types of ordering in the NP domains that may impact the stability of different microphase structures. This is an area for future study.

Conclusion. In this paper, we explored the phase behavior of a system of immiscible NP spheres tethered to one another, altering both the diameter ratio of the NPs and the length of the tether. Each configuration was simulated over a range of volume fractions and temperatures. We found long micelle, network, micelle in network, lamellae, and perforated lamellar phases. All phases reported as equilibrium phases in the triblock copolymer literature also appear in this TNPT system. In addition, we report three phases that are new to the design space: β -Sn micelless in network, *R* $\bar{3}$ *m* micelles, and honeycomb with short and long micelles.

Varying both the diameter ratio and tether length have a significant impact on the self-assembled phases. First, as the diameter ratio deviates from 1.0, the asymmetry in the NP end group volume fractions stabilizes asymmetric phases. Second, increasing the tether length increases the number and complexity of the phases present. A longer tether provides the TNPT system more freedom to satisfy energetic constraints such as the bonding of incompatible NP end groups and the asymmetric NP sizes. The most complex phases (β -Sn micelle in network, double gyroid, *Fddd*, *R* $\bar{3}$ *m* phases) are found when the diameter ratio is asymmetric and the tether is long. We have introduced a new set of complex structures that can be spontaneously self-assembled from tethered nanoparticles and thereby comprise materials other than polymer. Only simple nanospheres of different sizes are required to create these complex phases. For future studies, we theorize that adding additional constraints to the system, such as changing the shape of the nanoparticles to disrupt the packing⁵¹ in the end group domains, may lead to new complex phases possessing hierarchies of order.

■ AUTHOR INFORMATION

Corresponding Author

*E-mail: sslotzer@umich.edu.

■ ACKNOWLEDGMENTS

The author thanks Ben Schultz for help with cluster detection and Michael Engel for his assistance identifying the β -Sn phase. Research supported by the U.S. Department of Energy, Office of Basic Energy Sciences, Division of Materials Sciences and Engineering under Award #DE-FG02-02ER46000. CLP was supported by the U.S. Department of Energy, Office of Basic Energy Sciences, Division of Materials Sciences and Engineering, under award DE-FG02-02ER46000, the U.S. Department of Energy Computational Science Graduate Fellowship and U.S. Department of Energy, Office of Science, under Contract DE-AC02-06CH11357. C.L.P. was funded by the Office of the Director through the Named Postdoctoral Fellowship Program (Aneesur Rahman Postdoctoral Fellowship), Argonne National Laboratory.

■ REFERENCES

- (1) Maldovan, M.; Thomas, E. L. *Nat. Mater.* **2004**, *3*, 593–600.
- (2) Saranathan, V.; Osuji, C.; Mochrie, S.; Noh, H.; Narayanan, S.; Sandy, A.; Dufresne, E.; Prum, R. *Proc. Natl. Acad. Sci. U.S.A.* **2010**, *107*, 11676–11681.
- (3) Saba, M.; Thiel, M.; Turner, M.; Hyde, S.; Gu, M.; Gross-Brauckmann, K.; Neshev, D.; Mecke, K.; Schröder-Turk, G. *Phys. Rev. Lett.* **2011**, *106*, 103902.
- (4) Lin, B. J. *J. Microlith., Microfab., Microsyst.* **2004**, *3*, 377–395.
- (5) Jankowski, E.; Marsh, H. S.; Jayaraman, A. *Macromolecules* **2013**, *46*, 5775–5785.
- (6) Turner, M. D.; Saba, M.; Zhang, Q.; Cumming, B. P.; Schröder-Turk, G. E.; Gu, M. *Nat. Photonics* **2013**, *1*–5.
- (7) Scherer, M. R. J.; Steiner, U. *Nano Lett.* **2012**, *13*, 3005–10.
- (8) Whitesides, G. M.; Grzybowski, B. *Science* **2002**, *295*, 2418–21.
- (9) Glotzer, S. C.; Solomon, M. J. *Nat. Mater.* **2007**, *6*, 557–62.
- (10) Nie, Z.; Petukhova, A.; Kumacheva, E. *Nat. Nanotechnol.* **2010**, *5*, 15–25.
- (11) Zhang, Z.; Horsch, M. A.; Lamm, M. H.; Glotzer, S. C. *Nano Lett.* **2003**, *3*, 1341–1346.
- (12) Alivisatos, A. P.; Johnsson, K. P.; Peng, X.; Wilson, T. E.; Loweth, C. J.; Bruches, M. P., Jr.; Schultz, P. G. *Nature* **1996**, *382*, 609–11.
- (13) Zheng, J.; Constantinou, P. E.; Micheel, C.; Alivisatos, A. P.; Kiehl, R. A.; Seeman, N. C. *Nano Lett.* **2006**, *6*, 1502–4.
- (14) Nykypanchuk, D.; Maye, M. M.; van der Lelie, D.; Gang, O. *Nature* **2008**, *451*, 549–52.
- (15) Jones, M. R.; Macfarlane, R. J.; Lee, B.; Zhang, J.; Young, K. L.; Senesi, A. J.; Mirkin, C. A. *Nat. Mater.* **2010**, *9*, 913–7.
- (16) Cigler, P.; Lytton-Jean, A. K. R.; Anderson, D. G.; Finn, M. G.; Park, S. Y. *Nat. Mater.* **2010**, *9*, 918–22.
- (17) Maye, M. M.; Kumara, M. T.; Nykypanchuk, D.; Sherman, W. B.; Gang, O. *Nat. Nanotechnol.* **2010**, *5*, 116–20.
- (18) Macfarlane, R. J.; Lee, B.; Jones, M. R.; Harris, N.; Schatz, G. C.; Mirkin, C. a. *Science* **2011**, *334*, 204–208.
- (19) Wang, Y.; Wang, Y.; Breed, D. R.; Manoharan, V. N.; Feng, L.; Hollingsworth, A. D.; Weck, M.; Pine, D. J. *Nature* **2012**, *491*, 51–5.
- (20) Senesi, A. J.; Eichelsdoerfer, D. J.; Macfarlane, R. J.; Jones, M. R.; Auyeung, E.; Lee, B.; Mirkin, C. A. *Angew. Chem.* **2013**, *S2*, 6624–6628.
- (21) Feng, L.; Dreyfus, R.; Sha, R.; Seeman, N. C.; Chaikin, P. M. *Adv. Mater.* **2013**, *25*, 2779–2783.
- (22) Halverson, J. D.; Tkachenko, A. V. *Phys. Rev. E* **2013**, *87*, 062310.
- (23) Zhang, Y.; Lu, F.; Yager, K. G.; van der Lelie, D.; Gang, O. *Nat. Nanotechnol.* **2013**, *8*, 865–872.

- (24) Yu, X.; Zhang, W.-B.; Yue, K.; Li, X.; Liu, H.; Xin, Y.; Wang, C.-L.; Wesdemiotis, C.; Cheng, S. Z. *D. J. Am. Chem. Soc.* **2012**, *134*, 7780–7.
- (25) Dong, X.-H.; Zhang, W.-B.; Li, Y.; Huang, M.; Zhang, S.; Quirk, R. P.; Cheng, S. Z. *D. Polym. Chem.* **2012**, *3*, 124–134.
- (26) Yue, K.; Liu, C.; Guo, K.; Wu, K.; Dong, X.-H.; Liu, H.; Huang, M.; Wesdemiotis, C.; Cheng, S. Z. D.; Zhang, W.-B. *Polym. Chem.* **2013**, *4*, 1056–1067.
- (27) Yu, X.; Yue, K.; Hsieh, I.-f.; Li, Y. *Proc. Natl. Acad. Sci. U.S.A.* **2013**, *110*, 10078–10083.
- (28) Capone, B.; Coluzza, I.; LoVerso, F.; Likos, C. N.; Blaak, R. *Phys. Rev. Lett.* **2012**, *109*, 238301.
- (29) Kolb, H. C.; Finn, M. G.; Sharpless, K. B. *Angew. Chem.* **2001**, *40*, 2004–2021.
- (30) Horsch, M. A.; Zhang, Z.; Iacobella, C. R.; Glotzer, S. C. *J. Chem. Phys.* **2004**, *121*, 11455–62.
- (31) Glotzer, S. C.; Horsch, M. A.; Iacobella, C. R.; Zhang, X. L.; Chan, E.; Zhang, X. *Curr. Opin. Colloid Interface Sci.* **2005**, *10*, 287–295.
- (32) Iacobella, C. R.; Horsch, M. A.; Zhang, Z.; Glotzer, S. C. *Langmuir* **2005**, *21*, 9488–94.
- (33) Horsch, M.; Zhang, Z.; Glotzer, S. *Phys. Rev. Lett.* **2005**, *95*, 1–4.
- (34) Horsch, M. A.; Zhang, Z.; Glotzer, S. C. *J. Chem. Phys.* **2006**, *125*, 184903.
- (35) Horsch, M. A.; Zhang, Z.; Glotzer, S. C. *Nano Lett.* **2006**, *6*, 2406–13.
- (36) Iacobella, C.; Keys, A.; Horsch, M.; Glotzer, S. *Phys. Rev. E* **2007**, *75*, 1–4.
- (37) Iacobella, C. R.; Horsch, M. A.; Glotzer, S. C. *J. Chem. Phys.* **2008**, *129*, 044902.
- (38) Nguyen, T. D.; Zhang, Z.; Glotzer, S. C. *J. Chem. Phys.* **2008**, *129*, 244903.
- (39) Iacobella, C. R.; Glotzer, S. C. *Nano Lett.* **2009**, *9*, 1206–11.
- (40) Iacobella, C. R.; Glotzer, S. C. *Soft Matter* **2009**, *5*, 4492–4498.
- (41) Horsch, M. A.; Zhang, Z.; Glotzer, S. C. *Soft Matter* **2010**, *6*, 945–954.
- (42) Phillips, C. L.; Iacobella, C. R.; Glotzer, S. C. *Soft Matter* **2010**, *6*, 1693–1703.
- (43) Hall, L. M.; Jayaraman, A.; Schweizer, K. S. *Curr. Opin. Solid State Mater. Sci.* **2010**, *14*, 38–48.
- (44) Goyal, S.; Escobedo, F. A. *J. Chem. Phys.* **2011**, *135*, 184902.
- (45) Matsushita, Y.; Hayashida, K.; Dotera, T.; Takano, A. *J. Phys.: Condens. Matter* **2011**, *23*, 284111.
- (46) Judas, J.; Kirkensgaard, K. *Interface Focus* **2012**, *2*, 602–7.
- (47) Kirkensgaard, J. J. K. *Phys. Rev. E* **2012**, *85*, 031802.
- (48) Kirkensgaard, J. J. K.; Evans, M. E.; de Campo, L.; Hyde, S. T. *Proc. Natl. Acad. Sci. U.S.A.* **2014**, 1–6.
- (49) Evans, M.; Robins, V.; Hyde, S. *Acta Crystallogr., Sect. A* **2013**, *A69*, 262–275.
- (50) Schröder-Turk, G. E.; de Campo, L.; Evans, M. E.; Saba, M.; Kapfer, S. C.; Varslot, T.; Grosse-Brauckmann, K.; Ramsden, S.; Hyde, S. T. *Faraday Discuss.* **2013**, *161*, 215–247.
- (51) Damasceno, P. F.; Engel, M.; Glotzer, S. C. *Science* **2012**, *337*, 453–457.
- (52) Chandler, D.; Weeks, J. *Science* **1983**, *220*, 787–794.
- (53) Grest, G.; Kremer, K. *Phys. Rev. A* **1986**, *33*, 3628.
- (54) Anderson, J.; Lorenz, C.; Travesset, A. *J. Comput. Phys.* **2008**, *227*, 5342–5359.
- (55) Anderson, J.; Glotzer, S. arXiv preprint arXiv:1308.5587 2013, 1–13.
- (56) <http://codeblue.umich.edu/hoomd-blue/>, accessed January 12, 2014.
- (57) <http://web.archive.org/web/20110722080716/http://cst-www.nrl.navy.mil/lattice/>, accessed January 19, 2014.
- (58) Meuler, A. J.; Hillmyer, M. A.; Bates, F. S. *Macromolecules* **2009**, *42*, 7221–7250.
- (59) Tyler, C.; Qin, J.; Bates, F.; Morse, D. *Macromolecules* **2007**, *40*, 4654–4668.
- (60) Imai, M.; Sakai, K.; Kikuchi, M.; Nakaya, K.; Saeki, A.; Teramoto, T. *J. Chem. Phys.* **2005**, *122*, 214906.
- (61) Matsen, M. W. *J. Chem. Phys.* **1998**, *108*, 785–796.
- (62) Mogi, Y.; Mori, K.; Matsushita, Y. *Macromolecules* **1992**, *25*, 5412–5415.
- (63) Dotera, T.; Hatano, A. *J. Chem. Phys.* **1996**, *105*, 8413.
- (64) Dotera, T. *Phys. Rev. Lett.* **2002**, *89*, 1–4.
- (65) Anderson, J.; Sknepnek, R.; Travesset, A. *Phys. Rev. E* **2010**, *82*, 1–11.
- (66) Sarić, A.; Bozorgui, B.; Cacciuto, A. *J. Phys. Chem. B* **2011**, *115*, 7182–9.
- (67) Tschierske, C. *Chem. Soc. Rev.* **2007**, *36*, 1930–70.
- (68) Imai, M.; Kawaguchi, A.; Saeki, A.; Nakaya, K.; Kato, T.; Ito, K.; Amemiya, Y. *Phys. Rev. E* **2000**, *62*, 6865–74.
- (69) Hajduk, D.; Harper, P.; Gruner, S. *Macromolecules* **1994**, *27*, 4063–4075.
- (70) Hamley, I. W.; Koppi, K. A.; Rosedale, J. H.; Bates, F. S.; Almdal, K.; Mortensen, K. *Macromolecules* **1993**, *26*, 5959–5970.
- (71) Grünwald, M.; Lutker, K.; Alivisatos, a. P.; Rabani, E.; Geissler, P. L. *Nano Lett.* **2012**, *13*, 1367–1372.
- (72) Cheng, X.; Lin, L.; E, W.; Zhang, P.; Shi, A.-C. *Phys. Rev. Lett.* **2010**, *104*, 1–4.
- (73) Wales, D. J.; Doye, J. *J. Phys. Chem. A* **1997**, *5639*, 5111–5116.